PHOTONIC SENSORS / Vol. 16, No. 2, 2026: 9560007

High-Precision and Large-Scale Identical Ultra-Weak FBG Sensors With OFDR

Xinyue YU[1,2], Meng XIA[3], Jinglin SUI[1,2], Xing LIU[1,2], Dexin BA[1,2*], and Yongkang DONG[1,2]

[1]*National Key Laboratory of Laser Spatial Information, Harbin Institute of Technology, Harbin 150001, China*

[2]*Zhengzhou Research Institute, Harbin Institute of Technology, Zhengzhou 450007, China*

[3]*Zhejiang Key Laboratory of 3D Micro/Nano Fabrication and Characterization, Westlake Institute for Optoelectronics, Hangzhou 311421, China*

[*]Corresponding author: Dexin BA E-mail: dexinba@hit.edu.cn

Abstract: To achieve the large-multiplexing capability, identical weak fiber Bragg grating (WFBG) sensors typically adopt a short grating length to reduce the reflectivity. However, the corresponding broadband reflection spectrum compromises the attainable wavelength-shift measurement precision. In this work, to overcome this limitation, an array of identical weak FBGs with extended grating lengths is employed, which facilitates the narrower bandwidth and improved spectral precision. Weaker refractive-index modulation is required in the FBGs with a longer grating length, which makes it harder to locate the individual FBG. A correlation-based algorithm is proposed for accurate WFBG localization, while the reflection signal is extracted using a window length precisely matched to the physical grating length for the suppression of the system noise. Experimental results using an array with 4 000 identical WFBGs, each WFBG with a 10 mm grating length, demonstrate the strain measurement precision of 3.92 με. The proposed approach effectively balances the requirements for the high sensor density and high measurement precision, enabling practical applications for real-time structural health monitoring and high-precision sensing systems.

Keywords: Optical frequency domain reflectometer; weak fiber Bragg grating; ultra-weak refractive index modulation; correlation-based WFBG finding algorithm; high-precision interrogation

Citation: Xinyue YU, Meng XIA, Jinglin SUI, Xing LIU, Dexin BA, and Yongkang DONG, “High-Precision and Large-Scale Identical Ultra-Weak FBG Sensors With OFDR,” *Photonic Sensors*, 2026, 16(2): 9560007.

1. Introduction

Over the past several decades, optical fiber-based distributed sensors have attracted significant attention. Fiber Bragg gratings (FBGs) have been widely utilized as strain and temperature sensors due to their immunity to electromagnetic interference, linear response over a wide temperature and strain measurement range, and ease of handling and small sizes [1–8]. In particular, identical weak FBGs (WFBGs) with such low reflectivity are handy for fabrication and large-scale multiplexing and have the booming development in a fiber-optic sensor network, enabling quasi-

Received: 19 November 2025 / Revised: 30 December 2025
©The author(s) 2026. Published by Tsinghua University Press. This is an open access article under the Creative Commons Attribution 4.0 International License (http://creativecommons.org/licenses/by/4.0/)
DOI: 10.26599/PhoS.2026.9560007
Article type: Research article

distributed sensing over long distances with high spatial resolution. Among the interrogation schemes, the optical frequency domain reflectometry (OFDR) technique emerged as a promising approach used to monitor the reflection spectra of FBGs and then monitor their central wavelengths, which generally have a linear relationship with the variation of physical quantities [9–14]. The combination of the OFDR and WFBGs provides advantages in the multiplexing capability, simplicity of interrogation, and cost-effectiveness, with the capability of simultaneous localization and sensing in the OFDR system.

Weak reflectivity is essential for enabling large-scale multiplexing in wavelength-shift-based sensing systems. To achieve this, most previous efforts devoted to the OFDR sensing system were based on the multiplexed WFBG sensor array with a short grating length, while resulting in a broader reflection spectrum and compromised measurement precision. Gui *et al*. [15] demonstrated a dense ultra-short WFBG array with a grating length of 1 mm, achieving 1.5 mm spatial resolution along a 10 m fiber, with the temperature and strain accuracy of 1.00 ℃ and 20.02 με, respectively. Gui *et al*. [16] introduced random variation in both grating spacing and the central wavelength, maintaining a 1 mm grating length, and successfully interrogated 10 000 WFBGs in a single mode fiber (SMF). For wide-range strain sensing, Fu *et al*. [17] employed 1 mm femtosecond-laser-inscribed WFBGs to achieve a 10 000 με measurement range with 5 mm spatial resolution. Additionally, a 2 mm-long WFBG array had been inscribed in multicore fibers, enabling accurate two-dimensional and three-dimensional shape reconstruction [18]. However, the spectral broadening due to the physical grating length inherently degraded the wavelength resolution and limited the sensing precision. Contrarily, the WFBG of a longer grating length can narrow the spectral bandwidth and improve the theoretical precision, while ultra-weak refractive modulation is required to maintain low reflectivity. Hence, it is desirable to achieve high precision demodulation while preserving the optimal spectral performance in WFBG-based OFDR systems, particularly targeting those high-precision distributed sensing with the large-scale multiplexing capability.

In this paper, we demonstrate a high-precision distributed sensor based on an array of 4 000 identical WFBGs with the low reflectivity and extended grating length in the OFDR system. The optical interference signal is theoretically analyzed considering each reflector within the FBG distributed region and associated system noise. The influence of refractive index modulation of the FBG on the signal to noise ratio (SNR) is analyzed, particularly for WFBGs with ultra-weak refractive index modulation. To enhance the demodulation precision, a distance-domain signal extraction method based on the correlation is proposed and verified to precisely locate WFBGs and effectively suppress the system noise. The proposed demodulation strategy is experimentally validated using an array of 4 000 identical WFBGs with a grating length of 10 mm, the low peak reflectivity of −40 dB, and a uniform grating interval of 10 mm along the SMF, achieving the strain measurement precision of 3.92 με.

2. Principle of operation

2.1 Theoretical analysis

In an OFDR system based on an FBG array, as shown in Fig. 1(a), the output power of the tunable laser source (TLS) is split into two paths by the optical coupler (OC), and the test FBG array is placed in one path of the interferometer based on the Mach-Zehnder configuration. The spacing and grating lengths of FBGs are L and the reflectivity is r. The beat signal of the main Mach-Zehnder interferometer (MZI), which is the sum of the reference light and a series of reflected light generated from the WFBG array, is obtained by photodetector (PD), and the intensity of the beat signal in the MZI can be expressed as

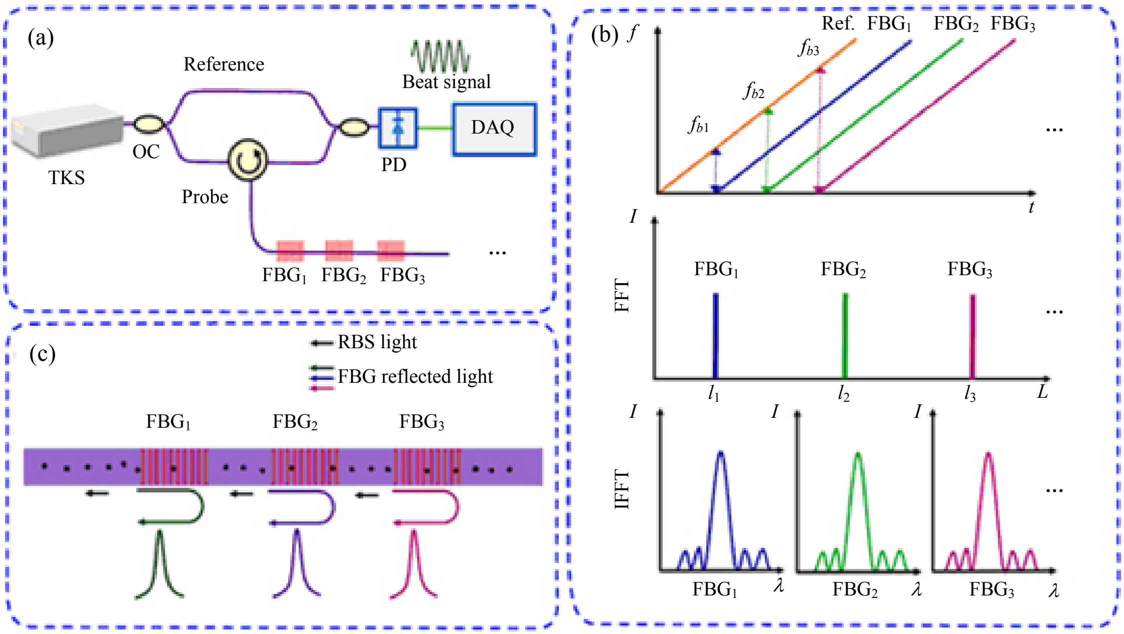

Fig. 1 Basic schematic of the WFBG-based OFDR system: (a) the basic configuration of the proposed FBG array-based OFDR system (DAQ: data acquisition card), (b) the demodulation principle of an OFDR-based wavelength demodulation system, and (c) the schematic of the FBG reflected light and RBS light in the identical FBG array.

$$I(t)=\left|E_R(t)+\sum_{n=1}^{N} r_n E_{\mathrm{pn}}(t-\tau_n)\right|^2 \quad (1)$$

where I is the intensity of the beat signal, E_R and E_{pn} are electric fields of the reference light and the nth reflected light, t is the time variable, N is the total number of WFBGs, and r_n and τ_n are the reflectivity and time delay of the nth WFBG in the array, respectively. The electric field of the reference light can be expressed as

$$E_R(t)=E_{R0}\exp[\mathrm{j}\varphi(t)] \quad (2)$$

where E_{R0} is the incident amplitude in the MZI, and φ is the phase of the reference light, which can be expressed as

$$\varphi(t)=2\pi f_0 t+\pi\gamma t^2+\varphi_0 \quad (3)$$

where f_0 is the initial frequency of the TLS, and φ_0 is the initial phase of incident light. The propagation model of the FBG reflected light and the Rayleigh backscattering (RBS) light in the FBG array is shown in Fig. 1(c). In fact, the reflected light in the probe path includes the FBG reflected light and RBS light. The former is generated by the heterogeneity of refractive index modulation due to the photosensitive property, while the latter RBS reflected signal is produced by molecular scale defects at the slight dopant level in the fiber medium, which have a significant difference in intensity.

Considering the reflected signal with the intrinsic RBS in the SMF and the extrinsic RBS enhancement in the written FBG region, the optical interference signal can be expressed as

$$I(t)=\left|E_R(t)+\sum_{n=1}^{N} r_n E_{\mathrm{pn}}(t-\tau_n)+\sum_{m=1}^{M} r_m E_{\mathrm{pm}}(t-\tau_m)\right|^2 \quad (4)$$

where E_{pm} and τ_m represent the electric field of reflected light and time delay generated by the mth scattering point, r_m represents the reflectivity of the mth scattering point, and M is the total number of the RBS points along the SMF. However, this formula cannot be used to describe the different characteristics between the FBGs with the same reflectivity but different grating lengths. In order to improve the characterization of the beat signal in the MZI more accurately, we proceed to modify (4) in terms of each reflector in the WFBG region, the optical interference signal can be expressed as

$$I(t)=\left|E_R(t)+\sum_{n=1}^{N}\sum_{k=1}^{K}r_{n,k}E_{\mathrm{pn}}(t-\tau_{n,k})+\sum_{m=1}^{M}r_mE_{\mathrm{pm}}(t-\tau_m)\right|^2 \quad (5)$$

where K is the total number of reflectors in one WFBG, $r_{n,k}$ and $\tau_{n,k}$ are the reflectivity and time delay of the kth reflector in the nth WFBG. Combining with the above equations, the beat signal of the reference light and the reflected light by the WFBG is submerged in the system noise originating from the interference between the reference light and RBS light, RBS light and FBG reflected light, and each FBG reflected light. The amplitude of $r_{n,k}$ in the FBG region and r_m of the RBS in the SMF are related to the SNR of the beat signal, and the SNR increases as the ratio of $r_{n,k}$ to r_m increases. A fast Fourier transform (FFT) is applied to the interference signal, and the power spectra can be resolved in the distance domain, as shown in Fig. 1(b). By using the inverse fast Fourier transform (IFFT), the selected WFBG in the distance domain is extracted through a sliding window and transformed back to the wavelength domain, and thus the optical wavelength spectrum of each FBG sensor in the identical FBG array could be obtained. To avoid the spectrum leakage, the Hanning window is employed.

The peak reflectivity of the FBG can be expressed as

$$R_{\max}=\tanh^2(\kappa\cdot L) \quad (6)$$

$$\kappa=\frac{\pi}{\lambda}\int_{-\infty}^{\infty}\int_{-\infty}^{\infty}\Delta n(x,y)E(x,y)E^*(x,y)\mathrm{d}x\mathrm{d}y \quad (7)$$

where κ is the coupling coefficient, L is the grating length, Δn is the magnitude of the localized refractive index modulation in the FBG, $E(x,y)$ is transverse electric field distribution in the SMF. The coupling coefficient is defined by the refractive index modulation depth, as well as the coupling area between the refractive index modulation and mode field. Therefore, the amplitude of the RBS light enhanced by the FBG is directly connected to the refractive index modulation introduced in the FBG written region, instead of reflectivity itself. The greater the refractive index modulation is, the more visible the FBG reflected signal in the distance domain is, resulting in a higher SNR during demodulation.

2.2 Simulation of the large-scale WFBG array in the OFDR system

In order to investigate the influence of the width of the employed Hanning window on the demodulated IFFT spectrum, we further simulate the beat signal obtained in the OFDR system considering 4 000 WFBGs and the ground noise in the 100 m SMF, combining with the above equations. In this situation, the ratio of $r_{n,k}$ to r_m is so low that the reflected signal is slightly enhanced by the WFBG. Here, taking the first WFBG placed at a distance of 1 m for example, the grating length is set to 10 mm. The RBS noise is considered in simulation as the ground noise. Considering the practical dynamic range of the data acquisition card, the white Gaussian noise is also added as the spurious noise.

Considering the WFBG with the low peak reflectivity of −40 dB to provide the multiplexing capability in the application, the simulated beat signal in the distance domain after the FFT operation on the original beat signal is displayed in Fig. 2(a). The close view of the WFBG reflected signal is shown in the inset, roughly 10 dB enhanced due to the ultra-weak refractive index modulation of the WFBG in the fiber medium. The grating length and spacing in the WFBG array are consistent with the simulation parameters. Next, the Hanning window is employed to extract the WFBG reflected signal, and then applying IFFT on the extracted data. As illustrated in Figs. 2(b1) and 2(b2), we place 20 mm-long and 10 mm-long Hanning windows at the center of the reflected signal, including one WFBG reflection, respectively. As depicted in

Figs. 2(c1) and 2(c2), the Bragg wavelength demodulation error is 12.90 pm captured by the 20 mm-long Hanning window compared to the theoretical Bragg wavelength derived by the transfer matrix model, which is more than 8.68 pm using a 10 mm signal. The demodulated Bragg wavelength has a minor deviation mainly attributed to different SNRs owing to the noise component in the employed window, particularly for the WFBG with ultra-weak refractive index modulation, which has poor amplitude contrast compared with the system noise floor. As a result, the irrelevant ground noise components should be minimized during demodulation.

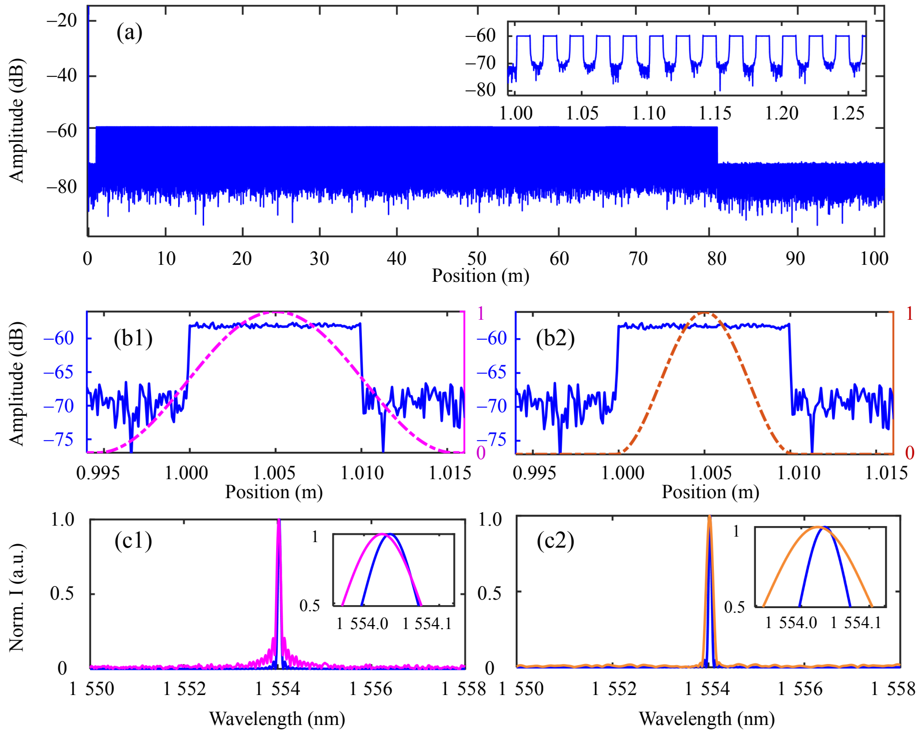

Fig. 2 Simulation of the sensing system using the WFBG sensor based on the OFDR: (a) the simulation result of the beat signal (on the logarithm scale) in the distance domain; the illustration of the selected WFBG section and the Hanning window whose width is (b1) 20 mm, (b2) 10 mm; the carmine line in (c1) and orange line in (c2) denote the normalized reflection spectra of the WFBG corresponding to (b1) and (b2) (the blue line represents the theoretical reflectivity spectrum of the WFBG based on the transfer matrix model).

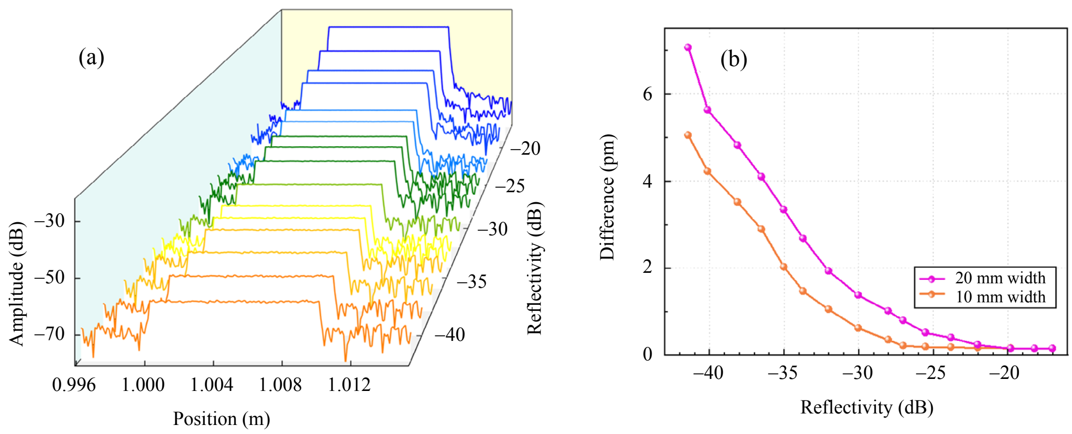

Fig. 3 Demodulation results of the WFBG with different refractive index modulation depths: (a) simulated power spectra of the beat signal (on the logarithm scale) in the distance domain using the FBG with increasing refractive index modulation and (b) difference values of IFFT demodulation results extracted by the 10 mm-long and 20 mm-long Hanning windows in each simulation.

Furthermore, an FBG of 10 mm is employed without the loss of generality, in order to investigate the influence of the refractive index modulation depth on the demodulated IFFT results. Figure 3(a) illustrates the simulation beat signal in the distance domain, which has the different amplitude contrast between the system noise floor and FBG reflected signal, corresponding to the variable SNR of the demodulated signal. It is demonstrated that the reflectivity of the FBG ranges from −41.5 dB to −17 dB due to the increasing refractive index modulation in the fiber medium. The WFBG reflected signal is retrieved using the 10 mm-long and 20 mm-long Hanning windows, applying the IFFT on the extracted data. The difference between IFFT demodulation results captured by different sizes and the theoretical Bragg wavelength of the FBG reflected signal is shown in Fig. 3(b). The difference of demodulation results approaches 0 when the reflectivity reaches −20 dB in this simulation. While the system noise has significant influence on demodulation performance, owing to the weak refractive index modulation and the employed window when reflectivity below −35 dB. Hence, it is necessary to suppress the system noise to improve the SNR of the demodulated signal for the WFBG array with ultra-weak refractive index modulation. Each WFBG should be precisely identified submerged from the noise ground and captured by the Hanning window of the same grating length.

3. Experimental validation for high-precision interrogation of WFBG array

3.1 Experimental setup and signal acquisition

Figure 4(a) provides the basic configuration of the proposed OFDR-based wavelength interrogation system using a femtosecond-laser-inscribed WFBG array.

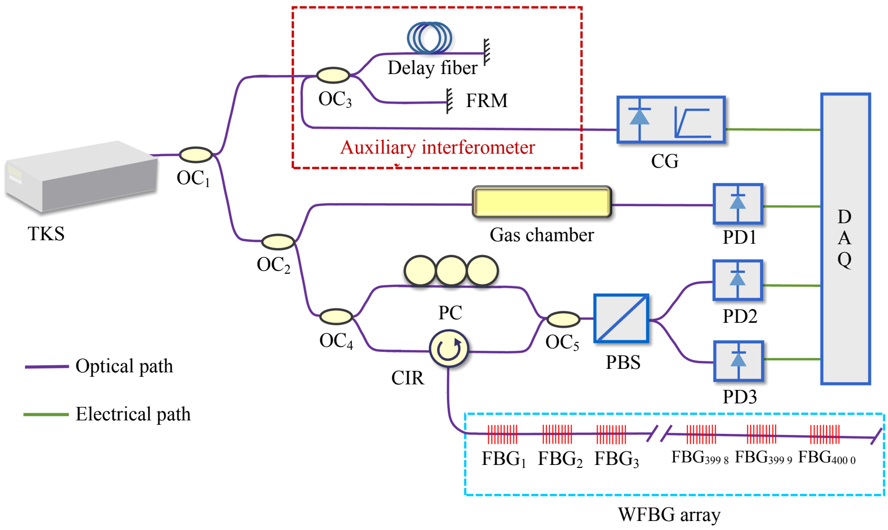

Fig. 4 Experimental setup for the OFDR-based interrogation system for a WFBG array: the WFBG array consisting of 4 000 identical WFBGs is inscribed in the SMF by the femtosecond laser point-by-point (FRM: faraday rotating mirror; CIR: circulator; PC: polarization controller; CG: clock generator; SMF: single mode fiber).

About 10% of the light enters into an auxiliary interferometer (AI) based on the Michelson configuration, which is used to compensate for the nonlinear phase noise of the TLS with a delay fiber of 200 m. The generated signal of the AI serves as the external clock of the DAQ to sample the interference signal from PDs 2 and 3 with equidistant optical frequency interval points. Hence, the maximum measurable distance of the main interferometer (MI) is about 100 m according to the Nyquist sampling theory. Two Faraday rotating mirrors (FRMs) in the Michelson configuration are used to reduce the polarization fading effect. The hydrogen cyanide (HCN) as an absorption gas chamber is adopted to calibrate the wavelength drift of the TLS. The remaining light is divided by a 1:99 OC_4 and enters into the MI. Then, the reflected light from the WFBG array interferes with the reference light passing through the PC at OC_5. The polarization beam splitter (PBS) is employed to reduce the polarization fading effects in the MI. In addition, the sweeping wavelength span of the TLS is 1 550 nm–1 560 nm with the sweeping rate of 100 nm/s and the output power of 5 mW. The WFBG array for the experiment consists of 4 000 identical WFBGs inscribed by the femtosecond laser direct writing technology.

The experimental results of the proposed OFDR system with the WFBG array consisting of 4 000 identical WFBGs are displayed in Fig. 5. As seen in Fig. 5(a), we can clearly see 4 000 bright reflected signals which correspond to 4 000 WFBGs in the sensor array. The average amplitude of reflected signal is slightly increased from −69.2 dB to −58.6 dB enhanced by the WFBG array. Figure 5(b) demonstrates an enlarged view of the beat signal, clearly showing that the measured grating length and spacing of the WFBG are 10 mm. Here, we select $WFBG_{69}$ as the reference, and Fig. 5(c) illustrates the IFFT spectra employing the 10 mm-long Hanning window and 20 mm-long Hanning window, depicted by orange and carmine curves, respectively. It is shown that the demodulated Bragg wavelengths using the 10 mm-long and 20 mm-long signals, respectively, have a slight deviation, corresponding to 1 553.848 nm and 1 553.842 nm, owing to the different SNRs of the extracted signal generated from the system noise.

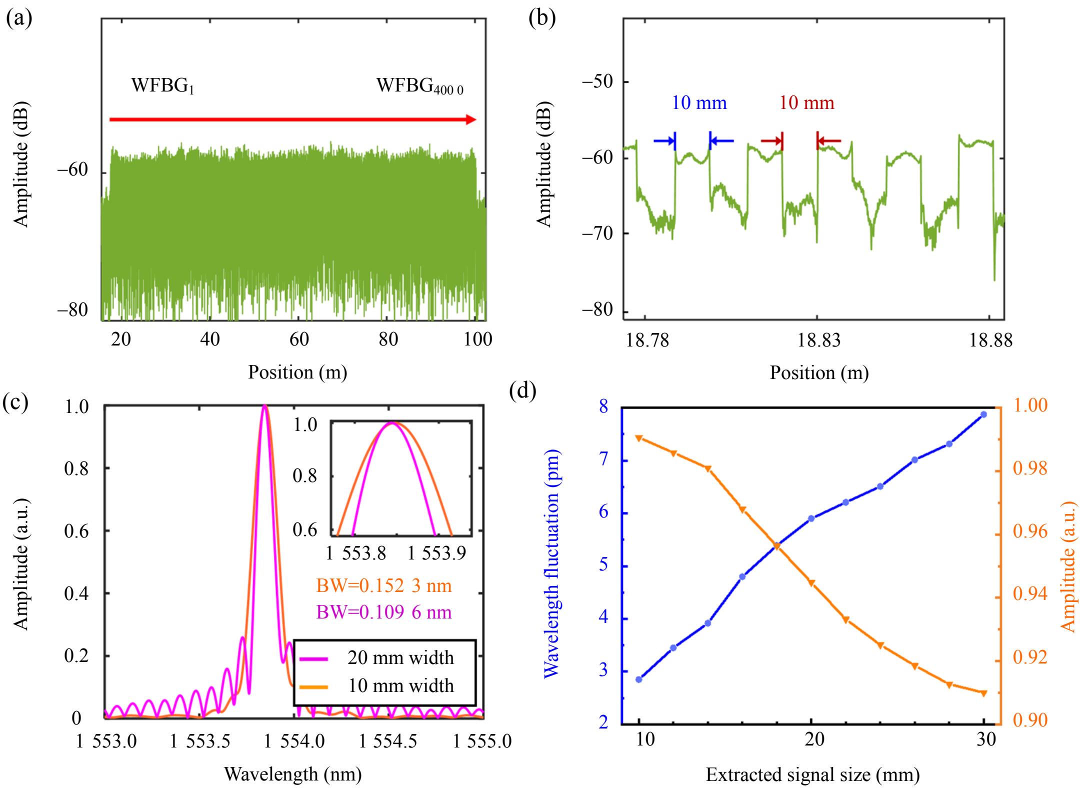

Fig. 5 Experimental result of the OFDR system with the WFBG array: (a) obtained power spectrum of the beat signal for the WFBG array in the SMF, (b) enlargement of the spectrum from $WFBG_{65}$ to $WFBG_{69}$ in (a), (c) the demodulated wavelength spectrum of $WFBG_{69}$ obtained by the 10 mm-long extracted signal and 20 mm-long extracted signal, and (d) the wavelength fluctuation by different sizes of windows in 20 replicate times of measurement depicted by the blue curve and the average amplitude of the cross-correlation coefficient of the WFBG69 spectrum depicted by the orange curve.

To evaluate the accuracy and stability of the sensing system, we further conduct 20 replicate times of measurement when the temperature and strain are held constant between scans. By increasing the Hanning window width from 10 mm to 30 mm with a step of 2 mm, the demodulated wavelength fluctuation gradually increases, as shown in Fig. 5(d). When the 10 mm WFBG signal is employed, the demodulated wavelength exhibits the least fluctuation. Additionally, since the cross-correlation algorithm is applied to derive the spectrum shift, the similarity of the demodulated spectrum is investigated. Figure 5(d) shows that the corresponding cross-correlation coefficient of the WFBG can be improved to 0.99, when the size of the signal for demodulation (i.e., the width of the Hanning window) is equal to the grating length of the WFBG. These results agree well with the theoretical discussions above.

3.2 Correlation-based WFBG finding algorithm processing

In general, the position of each FBG is always obtained by picking the Fourier peaks from the FFT spectra in the distance domain by use of the peak finding algorithm [16, 17]. Whereas, the enhancement of the intensity induced by the WFBG, with ultra-weak refractive index modulation is only about 10 dB greater than the system noise with the intense susceptibility to the noise, as illustrated in Fig. 5. Despite it is widely used in the WFBG-based OFDR system, the peak finding algorithm presents the complexity and error for identifying each WFBG submerged in the system noise, making the demand of WFBG signal precise extraction.

Here, we propose a novel correlation-based WFBG finding approach for high-precision identification of the WFBG. Notably, the reflected signal is clearly enhanced in the intensity because of the step change of the refractive index at both ends of each WFBG. To track the step changes in the intensity, a sliding rectangular window whose width is equal to the grating length is utilized to cross-correlate with the signal in the distance domain for WFBG detection from the beginning point, as illustrated in Figs. 6(a) and 6(b). When a pair of step changes in the WFBG signal coincides with the two sides of the sliding window, the cross-correlation coefficient reaches its maximum value. As a result, a certain maximum value of the cross-correlation coefficient is related to the single WFBG, which also corresponds to the central location of the WFBG shown in Fig. 6(c). In particular, the correlation-based WFBG finding algorithm involves five main steps:

Step 1. The exclusive distance domain for the WFBG array is segmented. The beginning and the finishing points of the WFBG finding process should be calibrated in accordance with the distance domain distribution of the first and the last WFBGs after the FFT.

Step 2. From the beginning point, a sliding window is employed to perform cross-correlation across the distance domain distribution within the single WFBG. The width and sliding ranges of the sliding window are determined by the known physical characteristics, specifically the length and spacing of the WFBG. The amplitude of the sliding window is 1.

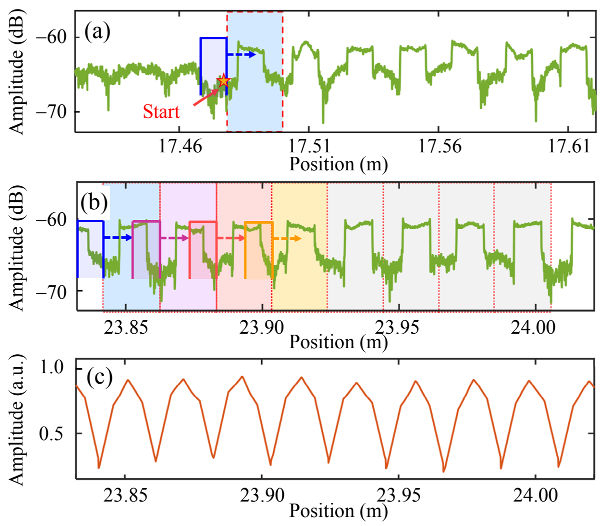

Fig. 6 Schematic diagram of the correlation-based WFBG finding algorithm: the red star in (a) is the beginning point of algorithm, (b) the sliding rectangular window is cross-correlated with the signal section containing one WFBG, and (c) the corresponding cross-correlated coefficient.

Step 3. Within this sliding range, the position of the WFBG is identified as the location corresponding to the maximum cross-correlation coefficient. And then, the $WFBG_1$ position is obtained naturally in the distance domain.

Step 4. The beginning point for the next iteration is determined based on the identified position of the $WFBG_1$. The sliding window for the WFGB finding is repositioned, and Steps 2 and 3 are executed to detect the subsequent WFBG ($WFBG_2$).

Step 5. The iterative process, including Steps 2, 3, and 4, continues until the sliding window reaches the pre-marked finishing point. The fluctuation in the obtained coefficients serves as an inspection standard, confirming the precise identification of each WFBG in the array.

According to the aforementioned steps, the positions of WFBGs in the array can be accurately retrieved by this correlation-based WFBG finding approach. The correlation-based WFBG localization eliminates the strict and unstable threshold, such as the peak interval and intensity provided in the peak-finding algorithm. This algorithm is theoretically appropriate for online positioning of the WFBG with various refractive index modulation and also be validated experimentally.

3.3 High-precision interrogation of WFBG array

In order to validate the accuracy of the correlation-based WFBG finding algorithm, each position of WFBGs is obtained by the aforementioned steps in the distance domain. Figure 7(a) demonstrates the comparison diagram between the position of the 4 000 WFBGs computed by the algorithm with the real position of WFBGs in the distance domain, where the cross-correlation coefficient is 1.00. The manual positioning of each WFBG is directly obtained from the distance domain

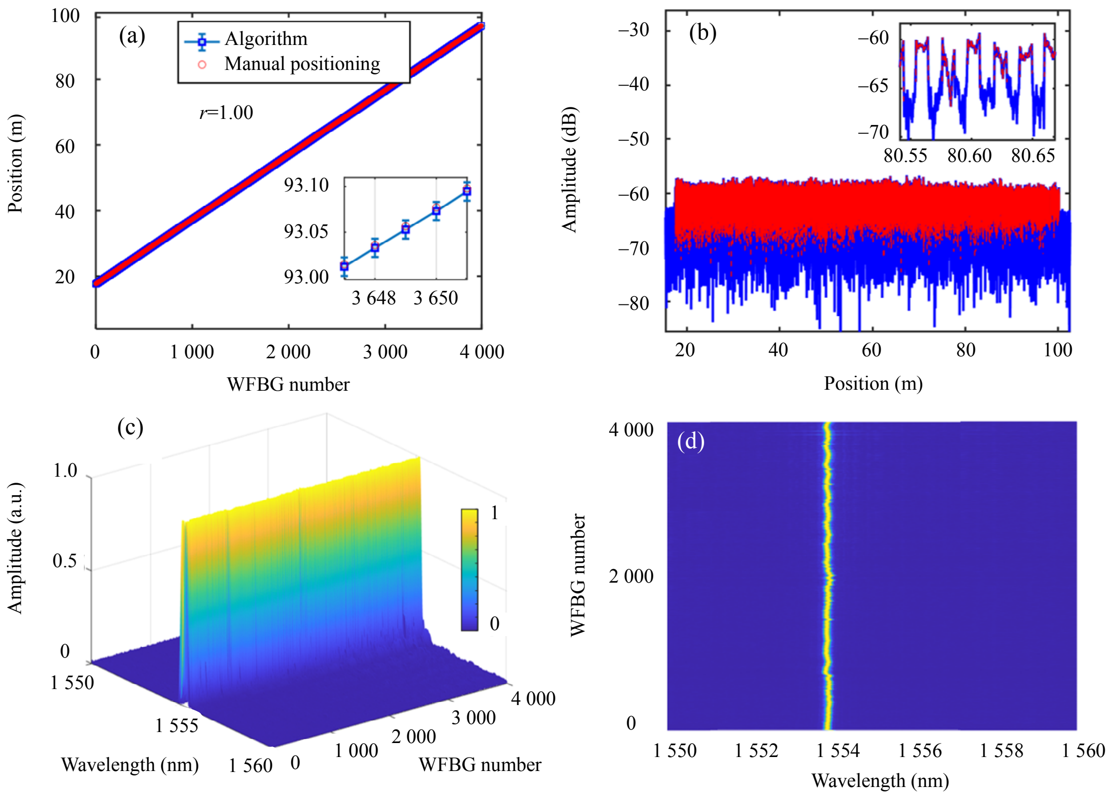

Fig. 7 High-precision interrogation of WFBG array: (a) obtained positions using the correlation-based WFBG finding algorithm (in blue) and the manually recorded positions (in red), (b) the distance domain result of the WFBG array depicted by the blue curve and the red dashed line represents the WFBG writing region obtained by the correlation-based algorithm, (c) wavelength spectra of all the 4 000 WFBGs in the array, and (d) the distribution of the demodulated Bragg wavelength for the WFBG array, ranging from 1 553.84 nm to 1 554.15 nm.

profile. All the 4 000 WFBGs' positions are accurately identified, as illustrated in Fig. 7(b). Despite the acquired signal showing degeneration compared to the simulated signal, the precise recognition of the WFBG position is still achieved in each experiment. Such strong robustness of the WFBG finding method provides the good tolerance for the deterioration of the reflected signal caused by the nonlinear effect and polarization effect in practice, and this method has the potential in versatile applications based on the WFBG. The Bragg resonance spectra of 4 000 WFBGs in the array are obtained by the IFFT operation with the 10 mm-long Hanning window, displayed in Fig. 7(c), and the distribution diagram of the demodulated Bragg wavelength is shown in Fig. 7(d), ranging from 1 553.84 nm to 1 554.15 nm. The variation reaches up to 0.31 nm, mainly caused by the power fluctuation of the laser and the inhomogeneity in the built-in stress within the fiber medium.

3.4 Strain sensing performance of WFBG array-based OFDR system

Furthermore, to investigate the strain sensing capability of the WFBG array, a strain of 5 000 με is applied to a 1 m-long WFBG array section. The ultraviolet (UV) glue is used to bind the two ends of the WFBG array to two one-dimensional micro-displacement platforms.

The strain is applied by adjusting one micro-displacement stage along the fiber axis between the $WFBG_{895}$ and $WFBG_{945}$, which corresponds to the position ranging from 35.37 m to 36.37 m. Figure 8(a) demonstrates the position of the partial WFBG array at 0 με and 5 000 με in the strained district. Notably, at the end of the strain district, the position of $WFBG_{944}$ shifts from 36.349 m to 36.355 m, owing to the 5 000 με strain-induced position deviation. We select $WFBG_{892}$ for the unstrained district and $WFBG_{940}$ for the strained district.

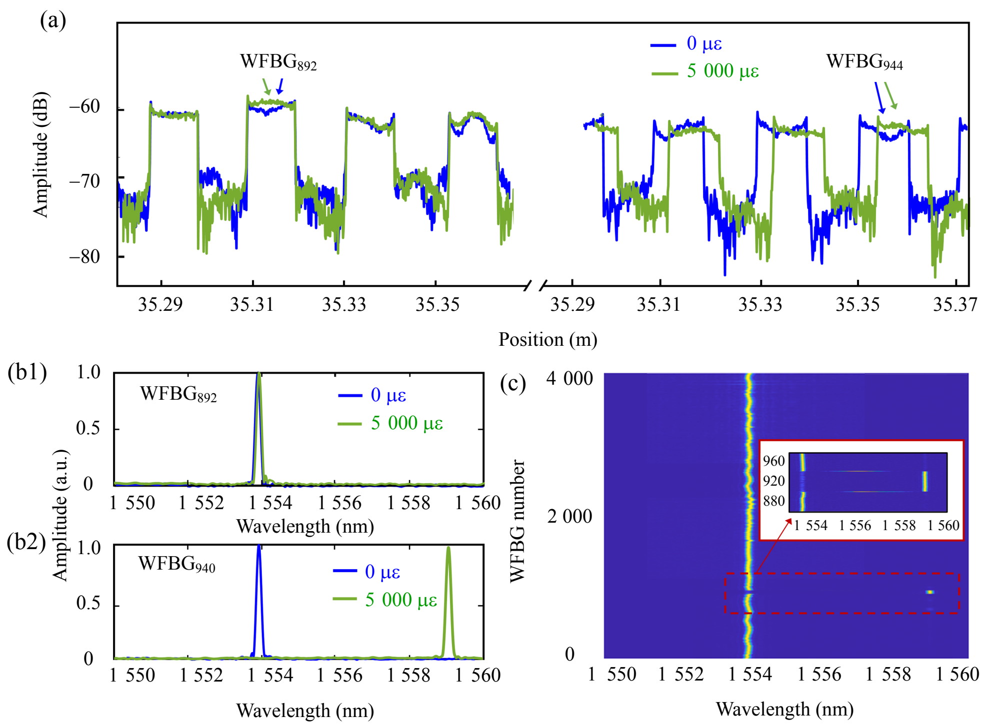

Fig. 8 Demodulation results of WFBGs under different strain conditions: (a) schematic of the position of the partial WFBG array under 0 με and 5 000 με strains in blue and green, respectively, and the wavelength spectra of (b1) the $WFBG_{892}$ outside the strain district and (b2) the $WFBG_{940}$ inside the strain district, and (c) the distribution of demodulated Bragg wavelengths under the 5 000 με strain.

As seen in Fig. 8(b), it is obvious that the wavelength spectrum of $WFBG_{892}$ exhibits almost the identical spectral shape and the Bragg wavelength of 1 553.91 nm. In the strain district, $WFBG_{940}$ has the similar spectral shape but different Bragg wavelengths due to the applied strain, corresponding to 1 553.91 nm and 1 559.19 nm. Besides, Fig. 8(c) depicts the distribution diagram of demodulated Bragg wavelengths for 4 000 WFBGs under the 5 000 με strain, exhibiting a noticeable Bragg wavelength shift in the strain region, consistent with the demodulation results in Fig. 8(b). The sensing spatial resolution is 20 mm in the OFDR system, which is equal to the grating length plus the spacing of each WFBG. Besides, it is remarkable that our WFBG finding algorithm has the robustness against the position deviation induced by the strain, so that each WFBG in a strain-applied district can be accurately determined in the distance domain.

Next, we proceed to investigate the measuring precision of the system. The applied strain is increased from 500 με to 5 000 με with a step of 500 με. The demodulated strain distribution can be reconstructed from the wavelength shift of each ultra-weak FBG in the array employing the 10 mm-long Hanning window, as shown in Fig. 9(a). Figure 9(b) presents the calibrated strain sensitivity coefficients from $WFBG_{895}$ to $WFBG_{945}$ in the strain district. Despite the strain performance in the WFBG array using the 20 mm-long and 10 mm-long Hanning windows could be clearly demodulated, minor variations in measurement errors primarily arise from the distinct SNR and noise component.

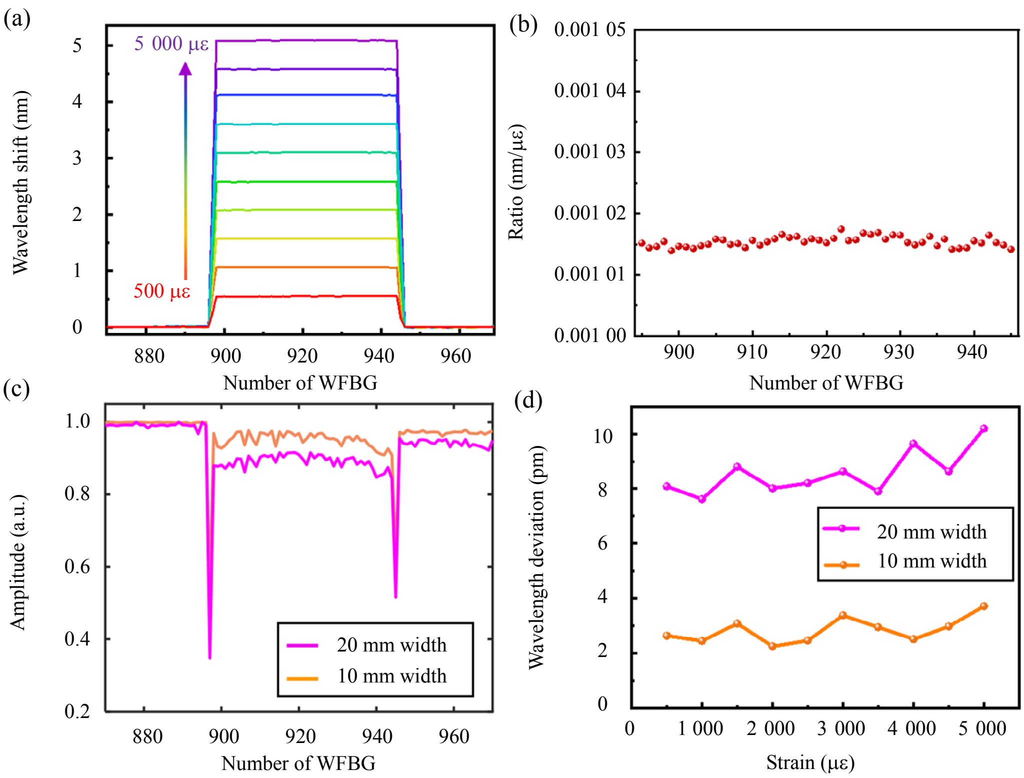

Fig. 9 Strain sensing performance of the WFBG array-based OFDR system: (a) the demodulated wavelength shift extracted of each WFBG by the 10 mm-long Hanning window, where the imposed strain is increased from 500 με to 5 000 με with a step of 500 με, (b) the ratio coefficients of WFBGs in the strain district, (c) the distributed amplitude of the cross-correlation coefficient under the strain of 5 000 με, and (d) the wavelength standard deviation of each measurement under the strain-applied district (the carmine and orange curves represent the 20 mm-long and 10 mm-long extracted signal, respectively).

We further calculate the average cross-correlation coefficient of the WFBG array demodulated by a 20 mm signal in 5 000 με during the demodulation, which is 0.890. It can be effectively increased to 0.951 by reducing the irrelevant noise demodulated by a 10 mm signal, thereby enhancing the SNR, as shown in Fig. 9(c). The standard deviations of strain distributions using the 20 mm-long and 10 mm-long Hanning windows, are depicted in Fig. 9(d), which are an indication of the imprecision of one time of individual measurement, corresponding to the strain precision of 9.89 με and 3.92 με under 5 000 με. It is shown that the demodulation error utilizing a 10 mm-long extracted signal significantly decreases compared with that using a 20 mm-long signal for demodulation, suggesting that the precise identification and extraction of the WFBG signal with the suppressed system noise provide a more precise demodulation result of the sensing system.

Table 1 summarizes the results of WFBG-based sensors in recent years, focusing on both demodulation precision with varying the grating lengths and multiplexing capability. Compared to 1 mm-WFBG sensors, the proposed interrogator achieves significantly higher measurement precision while maintaining competitive multiplexing capabilities. Different from interrogators utilizing the non-identical WFBG arrays, our approach employs the identical 10 mm WFBG array, which considerably simplifies the fabrication process and enhances practical feasibility. With the long grating length and larger-scale capability of the identical WFBG, the proposed interrogation system offers a novel and high-precision solution for positioning the WFBG and monitoring the corresponding wavelength shift. These advantages make the technique for applications demanding both the extensive spatial coverage and high measurement fidelity, such as structural health monitoring of the critical infrastructure and distributed environmental sensing networks.

Table 1 Performance comparison among WFBGs.

Grating length	Reflectivity	Multiplexing number	Precision	Identical or not	Ref.
1 mm	−40 dB	6 680	20.02 με	No	[15]
1 mm	<−45 dB	10 000	Unknown	No	[16]
Unknown	−37 dB	5 000	Unknown	Yes	[19]
0.07 nm (bandwidth)	Unknown	3 640	15 με	Yes	[20]
1 mm	−40 dB	110	Unknown	Yes	[17]
10 mm	−40 dB	4 000	3.92 με	Yes	This work

4. Conclusions

In summary, we demonstrate a high-precision, large-scale distributed sensing system based on an array of 4 000 identical ultra-weak FBGs interrogated using the OFDR. By employing an extended grating length of 10 mm, a narrower reflection bandwidth is achieved with enhanced theoretical wavelength resolution, but suffers from ultra-weak refractive index modulation and limited reflected signal amplitude. By selectively extracting signals matching the grating length of WFBGs, the proposed method is verified to the effectively suppress system noise contribution. A novel correlation-based WFBG finding algorithm is proposed for high-precision localization of each WFBG, thereby enhancing the SNR of the demodulated spectra. An array consisting of 4 000 identical WFBGs with the 10 mm grating length and −40 dB peak reflectivity is experimentally employed, achieving the strain sensing up to 5 000 με with the high precision of 3.92 με. Both theoretical and experimental results demonstrate that the proposed approach effectively improves the practicality and reliability of WFBG interrogation, offering a robust solution for large-scale and high-precision distributed sensing applications.

Acknowledgment

This work was supported in part by the National Key Research and Development Program of China (Grant No. 2023YFF0715803); in part by the Postdoctoral Scientific Research Development Fund of Heilongjiang province, China (Grant No. LBH-Q21092); in part by the National Key Laboratory of Laser Spatial Information Foundation, China (Grant No. LSI2024WDZC003); in part by the Construction Program for Basic Research of Characteristic Disciplines, China.

Declarations

Conflict of Interest The authors declare that they have no competing interests.

Permissions All the included figures, tables, or text passages that have already been published elsewhere have obtained the permission from the copyright owner(s) for both the print and online format.

Open Access This article is distributed under the terms of the Creative Commons Attribution 4.0 International License (http://creativecommons.org/licenses/by/4.0/), which permits unrestricted use, distribution, and reproduction in any medium, provided you give appropriate credit to the original author(s) and the source, provide a link to the Creative Commons license, and indicate if changes were made.

Use of AI Statement None.

References

[1] F. Peng and X. Cao, "A hybrid *Φ*/B-OTDR for simultaneous vibration and strain measurement," *Photonic Sensors*, 2016, 6(2): 121–126.

[2] W. Gao, J. Liu, H. Guo, X. Jiang, S. Sun, and H. Yu, "Multi-wavelength ultra-weak fiber Bragg grating arrays for long-distance quasi-distributed sensing," *Photonic Sensors*, 2022, 12(2): 185–195.

[3] Q. Cen, S. Pian, X. Liu, Y. Tang, X. He, and Y. Ma, "Microtaper leaky-mode spectrometer with picometer resolution," *eLight*, 2023, 3(1): 9.

[4] J. E. Fröch, L. Huang, Q. A. A. Tanguy, S. Colburn, A. Zhan, A. Ravagli, *et al.*, "Real time full-color imaging in a Meta-optical fiber endoscope," *eLight*, 2023, 3(1): 13.

[5] D. A. Nguyen, D. H. Kim, G. H. Lee, S. Kim, D. C. Shin, J. Park, *et al.*, "Real-time monitoring of fast gas dynamics with a single-molecule resolution by frequency-comb-referenced plasmonic phase spectroscopy," *PhotoniX*, 2024, 5(1): 22.

[6] L. Zhang, X. Shang, S. Cao, Q. Jia, J. Wang, W. Yan, *et al.*, "Optical steelyard: high-resolution and wide-range refractive index sensing by synergizing Fabry-Perot interferometer with metafibers," *PhotoniX*, 2024, 5(1): 24.

[7] L. Shao, J. Zhang, X. Chen, D. Xu, H. Gu, Q. Mu, *et al.*, "Artificial intelligence-driven distributed acoustic sensing technology and engineering application," *PhotoniX*, 2025, 6(1): 4.

[8] Z. Yang, X. Yan, B. Peng, Z. Li, X. Xia, C. Lu, *et al.*, "Ultrafast and reproducible fiber-optic hydrogen sensor via a tilted fiber grating with Pd/WO_3 nanocoating," *Photonic Sensors,* 2025, 15(2): 250229.

[9] J. Tang, L. Cai, C. Li, M. Yang, H. Guo, and W. Gan "Distributed acoustic sensors with wide frequency response based on UWFBG array utilizing dual-pulse detection," *Optical Fiber Technology*, 2021, 61: 102452.

[10] Z. Zhu, D. Ba, L. Liu, L. Qiu, S. Yang, and Y. Dong, "Multiplexing of Fabry-Pérot sensor by frequency modulated continuous wave interferometry for quais-distributed sensing application," *Journal of Lightwave Technology*, 2021, 39(13): 4529–4534.

[11] K. Liu, G. Yin, Z. Zhang, P. Yang, H. Lu, D. Li, *et al.*, "High-resolution and high-precision *Φ*-OFDR strain sensing scheme based on adaptive phase unwrapping and wavelet packet denoising," *Journal of Lightwave Technology*, 2024, 42(2): 891–897.

[12] X. Liu, Q. Li, X. Yu, Z. D. Ge, T. F. Li, and J. L. Sui, "Multi-point and high-sensitivity hydrogen sensor based on OFDR and fiber-tip microcavities," *Journal of Lightwave Technology*, 2025, 43(14): 6994–7000.

[13] X. Yu, S. Liu, X. Liu, J. Sui, Y. Zhou, H. Li, *et al.*, "Large-scale strain sensor based on a distance reposition method by permanent scatters in an OFDR system," *Optics Letters*, 2025, 50(17): 5414.

[14] Y. Yuan, W. Zhou, R. Wang, Y. Wang, Y. Dong, S. N. Burokur, *et al.*, "Non-orthogonal metasurfaces for channel-locked spin-orbital transitions," *Advanced Photonics*, 2025, 7(5): 056009.

[15] X. Gui, Z. Li, F. Wang, Y. Wang, C. Wang, S. Zeng, *et al.*, "Distributed sensing technology of high-spatial resolution based on dense ultra-short FBG array with large multiplexing capacity," *Optics Express*, 2017, 25(23): 28112.

[16] X. Gui, Z. Li, X. Fu, C. Wang, H. Wang, F. Wang, *et al.*, "Large-scale multiplexing of a FBG array with randomly varied characteristic parameters for distributed sensing," *Optics Letters*, 2018, 43(21): 5259.

[17] C. Fu, R. Sui, Z. Peng, Y. Meng, H. Zhong, R. Shan, *et al.*, "Wide-range OFDR strain sensor based on the femtosecond-laser-inscribed weak fiber Bragg grating array," *Optics Letters*, 2023, 48(21): 5819.

[18] C. Fu, S. Xiao, Y. Meng, R. Shan, W. Liang, H. Zhong, *et al.*, "OFDR shape sensor based on a femtosecond-laser-inscribed weak fiber Bragg grating array in a multicore fiber," *Optics Letters*, 2024, 49(5): 1273.

[19] H. Zhang, D. Fan, Y. Ma, Z. Xiong, Y. Pang, X. Chen, *et al.*, "Interrogation of 5000 ultraweak fiber Bragg grating sensors using optical frequency domain reflectometry," *Optical Engineering*, 2018, 57(10): 106110.

[20] J. Wang, Z. Li, Q. Yang, X. Fu, X. Gui, C. Wang, *et al.*, "Interrogation of a large-capacity densely spaced fiber Bragg grating array using chaos-based incoherent-optical frequency domain reflectometry," *Optics Letters*, 2019, 44(21): 5202.